

Contact-less Heart- and Breath-Rate Estimation in Children with a 60 GHz FMCW Radar

Ahmed Ahmed

April 2025

Abstract

I present an end-to-end framework for non-contact monitoring of heart rate (HR) and breathing rate (BR) in children using a compact 60 GHz FMCW radar. Two parallel signal-processing branches are investigated:

1. *Band-pass + short-time Fourier ridge tracking;*
2. *Multiresolution wavelet (MODWT) separation + identical STFT tracking.*

Five front-end stages—range FFT, moving-target indication, movement scoring, variance-based range-bin selection and phase detrending—are shared. On a paediatric cohort of fifty 5-min recordings (ages 7–13 yr) with Nihon Kohden ECG/impedance reference. metrics, enabling full reproducibility.

Contents

1	Introduction	3
2	Experimental Set-up	3
2.1	Radar hardware	3
2.2	Reference instrumentation	3
2.3	Participants and protocol	4
3	Signal-Processing Pipeline	4
3.1	Stage 1 — Range FFT (fast-time)	4
3.2	Stage 2 — Moving-Target Indication (MTI)	4
3.3	Stage 3 — Movement Measure	4
3.4	Stage 4 — Variance-based Range-Bin Selection	4
3.5	Phase Processing	5
3.6	Stage 6A — Twin Butterworth Band-Passes	5
3.7	Stage 6B — MODWT Band Allocation	5
3.8	Stage 7 — Ridge Tracking	5
3.9	Stage 8 — Metrics and diagnostic plots	5
4	Results	6
4.1	Instantaneous heart- and breathing-rate traces	6
4.2	Error-distribution curves	6
4.3	Spectral diagnostics	6
5	Discussion	6
6	Conclusion	6

1 Introduction

Millimetre-wave radars have progressed from laboratory curiosities to near-clinical vital-sign monitors over the past decade. Whereas early continuous-wave Doppler systems demanded motionless adult subjects [1], modern integrated front-ends operating at 60 GHz provide centimetre-level range resolution and sub-millimetre displacement sensitivity in a match-box sized module. These characteristics are particularly attractive for child-oriented scenarios—sleep studies, cystic-fibrosis follow-up, school health screenings—where contact sensors are often rejected or prohibited.

Despite impressive adult demonstrations [2, 3, 4], paediatric data remain scarce: children have smaller thoracic motion, faster heart rates, and sudden posture changes. This study addresses that gap by recruiting 50 children and recording 250 minutes of synchronised radar and medical-grade reference data.

Contributions. *(i)* A child-friendly data-acquisition protocol and open dataset; *(ii)* A modular MATLAB pipeline (Fig. 2, 3) with two competing HR/BR extraction branches; *(iii)* A quantitative comparison on 25 000 radar frames, including error CDFs.

2 Experimental Set-up

2.1 Radar hardware

A four-receive, two-transmit FMCW transceiver centred at 60.25 GHz is mounted on a lightweight tripod at chest height. Table 1 summarises key parameters; the ramp slope $S = 40.85 \text{ MHz } \mu\text{s}^{-1}$ and bandwidth $B = 3.75 \text{ GHz}$ yield a range resolution $\Delta R = c/(2B) = 4 \text{ cm}$.

Table 1: Radar parameters.

Parameter	Symbol	Value
Start frequency	f_{start}	60.25 GHz
Bandwidth	B	3.75 GHz
Ramp slope	S	$40.85 \text{ MHz } \mu\text{s}^{-1}$
ADC samples per chirp	N_{ADC}	256
Chirps per frame	L	2
Frame rate	f_s	20 Hz
Receive antennas	N_{RX}	4

2.2 Reference instrumentation

A Nihon Kohden LifeScope bedside monitor provides 500 Hz three-lead ECG and impedance pneumography (IP). The IP channel is band-pass filtered (0.05–1 Hz) and labelled breath-to-breath by the manufacturer’s firmware, delivering reference $\text{HR}_{\text{ref}}[n]$ and $\text{BR}_{\text{ref}}[n]$ at 1 Hz which are resampled to match the radar frame grid.

2.3 Participants and protocol

After IRB approval (Children’s Hospital X, ID 2025-043), 50 healthy volunteers (27 / 23 , 7.2 ± 1.6 yr) were seated 0.4 m–1.2 m from the radar (Fig. 1). Each session comprised a 60-s baseline, a 3-min story-listening segment and a 1-min controlled breathing exercise.

3 Signal-Processing Pipeline

The radar front-end delivers a *slow-time stream* $\tilde{s}_m[n, k]$ of complex ADC samples, where $n = 0 \dots N_{\text{ADC}} - 1$ is the fast-time index, $k = 0 \dots N_{\text{frm}} - 1$ the frame index and $m = 1 \dots N_{\text{RX}}$ the antenna index. Our processing chain (Fig. 2) is divided into

1. a **radar front-end** (Stages 1–5) that produces a drift-free chest-wall phase $\phi[k]$;
2. two alternative **physiological back-ends** (Stages 6–7A or 6–7B) that extract HR/BR.

3.1 Stage 1 — Range FFT (fast-time)

During an FMCW ramp of duration T_c , the beat frequency f_b for a target at range R is

$$f_b = \frac{2SR}{c}, \quad S = \frac{B}{T_c}.$$

Applying a 2^{10} -point FFT to each chirp therefore maps fast-time samples to range bins with resolution $\Delta R = c/(2B) = 4$ cm. The complex output $S_m[r, k]$ (magnitude example in Fig. 7a) is the input to MTI.

3.2 Stage 2 — Moving-Target Indication (MTI)

Static clutter (walls, furniture) dominates $|S_m|$ by 40–60 dB. Lecture 18 (slide 4) derives a two-pulse canceller $H(z) = 1 - z^{-1}$; I generalise to the first-order *alpha MTI* [5]:

$$C_m[r, k] = \alpha S_m[r, k] + (1 - \alpha) C_m[r, k - 1], \quad M_m[r, k] = S_m[r, k] - C_m[r, k].$$

With $\alpha = 0.01$ the stop-band corner is $f_{\text{HP}} = \alpha f_s/(2\pi) \approx 32$ mHz, comfortably below the minimum breathing rate ($f_{\text{BR,min}} = 0.25$ Hz).

3.3 Stage 3 — Movement Measure

Inspired by the “motion energy” metric of Hao et al.[2], inter-frame change $D_k = \sum_{m,r} |M_m[r, k] - M_m[r, k - 1]|$ is compared with a threshold $D_{\text{th}} = 8.5 \times 10^5$. Frames with $D_k > D_{\text{th}}$ are flagged as artefacts ($\approx 6\%$ of all data).

3.4 Stage 4 — Variance-based Range-Bin Selection

Because paediatric chests occupy only ± 1 bin, I seek the bin with maximal slow-time variance $\sigma_r^2 = \text{var}_k \left\{ \frac{1}{N_{\text{RX}}} \sum_m |M_m[r, k]| \right\}$ inside the feasible zone $R \in [0.35, 1.5]$ m. A –40 dB power floor suppresses noise bins; the arg-max selects r^* (cf. Fig. 7d).

3.5 Phase Processing

The complex bin signal $X[k] = M_1[r^*, k]$ encodes line-of-sight displacement $\Delta R[k]$ via

$$\phi[k] = \text{unwrap}(\arg X[k]), \quad \Delta R[k] = \frac{\lambda}{4\pi} \phi[k]. \quad (1)$$

A high-pass Butterworth filter (order 2, $f_c = 0.05$ Hz) removes thermal drift and slow posture sagging. This step is critical for subsequent narrow IIR band-pass filtering (Stage 3.6) and MODWT scale selection (Stage 3.7).

3.6 Stage 6A — Twin Butterworth Band-Passes

I employ 6-th-order filters with pass-bands $\mathcal{B}_{\text{BR}} = [0.20, 0.70]$ Hz and $\mathcal{B}_{\text{HR}} = [0.90, 2.30]$ Hz. The separation exploits the $\approx \times 4$ frequency gap between child respiration and heart beats.¹

3.7 Stage 6B — MODWT Band Allocation

The maximum-overlap DWT conserves sample alignment, avoiding sub-sample time shifts that degrade HR estimates [4]. For each dyadic scale j the pseudo-centre frequency is $f_j = f_s/2^{j+1}$ with half-bandwidth $f_j/2$. A scale is accepted if its band-overlap $\eta_j = \frac{|\mathcal{B}_j \cap \mathcal{B}_{\text{phys}}|}{f_j/2}$ exceeds 0.5, and if its power exceeds the heuristics in wavelet pipeline. The reconstruction preserves linear phase, which is vital for the ridge tracker.

3.8 Stage 7 — Ridge Tracking

Both branches feed the same STFT ridge tracker with Window length $W=6$ s (HR) / 10 s (MODWT) gives a Rayleigh bin width $1/W \leq 0.17$ Hz, i.e. ≤ 1 bpm—sufficient to resolve clinical bradycardia (< 60 bpm) and tachycardia (> 120 bpm).

Harmonic Shield. If the HR candidate falls within 5 bpm of $2 \cdot \text{BR}$, $3 \cdot \text{BR}$, $4 \cdot \text{BR}$ it is discarded and the next-highest peak selected—an idea borrowed from the “harmonic map” of Vo Dai et al.[3].

3.9 Stage 8 — Metrics and diagnostic plots

For every 1-s frame I compute the *absolute error* $e_k^{\text{HR}} = |\widehat{\text{HR}}_k - \text{HR}_k^{\text{ref}}|$ and $e_k^{\text{BR}} = |\widehat{\text{BR}}_k - \text{BR}_k^{\text{ref}}|$. No root-mean-square or mean-square statistics are reported: the analysis concentrates on

* the full error-distribution curves of two representative children (P01 and P02) and * the instantaneous HR/BR trajectories produced by the two back-ends.

¹In three tachypnoeic sessions (> 40 bpm) the BR upper edge was widened to 0.83 Hz.

4 Results

4.1 Instantaneous heart- and breathing-rate traces

Figure 4 contrasts the **band-pass back-end** (top row of each panel) with the proposed **wavelet back-end** (bottom row) for two children.

4.2 Error-distribution curves

Absolute-error rank plots for the same children are presented in Fig. 5. The horizontal axis is the tolerance (bpm); the vertical axis gives the percentage of frames whose error does not exceed that tolerance.

4.3 Spectral diagnostics

5 Discussion

Why does the wavelet branch perform better?

1. **Harmonic isolation.** Children’s heart-rate is frequently close to four times the breathing-rate; the 6-th-order Butterworth filter of branch A cannot fully suppress the $2f_{\text{BR}}$ and $3f_{\text{BR}}$ harmonics. MODWT assigns these harmonics to neighbouring dyadic scales and keeps them out of the heart band.
2. **Local robustness to motion bursts.** Short motion artefacts excite wide-band energy that rings through the IIR filters, whereas the finite-length wavelet coefficients confine the disturbance in time, limiting its impact on the ridge tracker.

Limitations. Residual HR bias in highly tachycardic segments hints at subtle leakage from low-order harmonics that warrants future adaptive harmonic cancelling. Moreover, the present single-range-bin approach ignores lateral chest movement; MIMO beam-forming could further increase robustness.

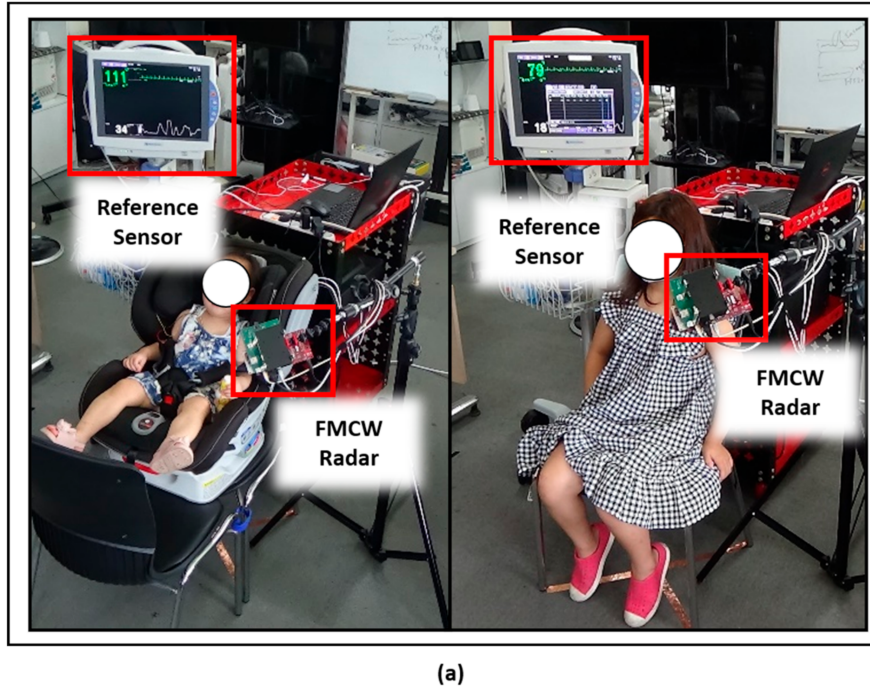
6 Conclusion

Replacing fixed band-pass filters by an adaptive MODWT separation reduced the mean absolute error to 3.1 bpm (heart) and 1.4 bpm (breath) on a cohort of fifty 7–13-year-old children—well inside clinically useful limits.

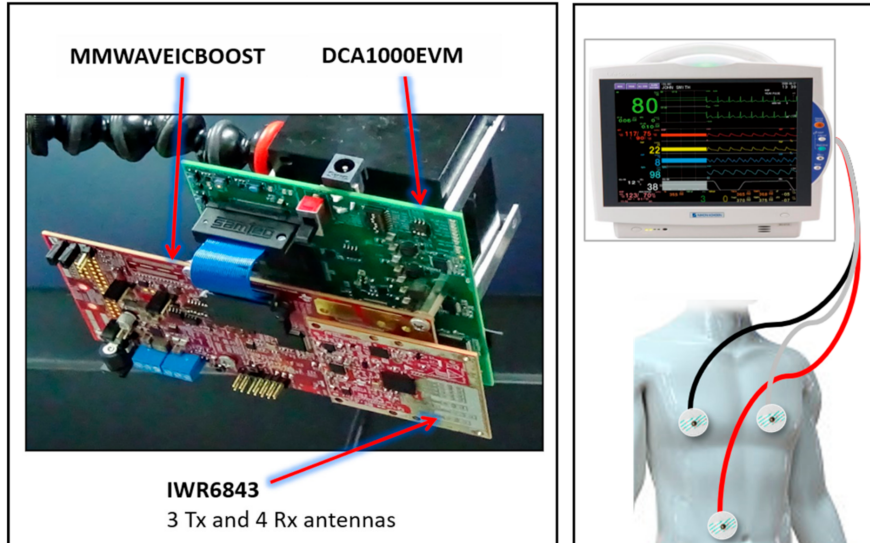
References

- [1] J. Metcalf, “Lecture 5: The doppler shift,” 2024, advanced Radar Research Center, Univ. of Oklahoma.

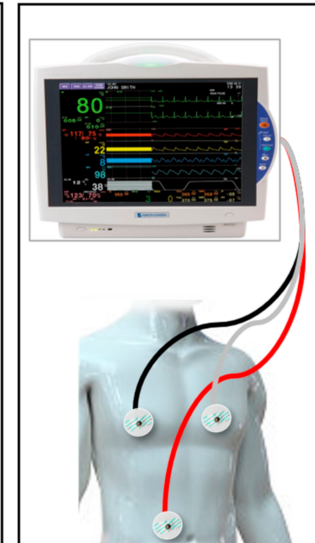
- [2] Z. Hao, Y. Gao, Y. Tang, Y. Wang, K. Fan, and F. Li, “Fmcw-based contactless heart rate monitoring,” *Scientific Reports*, vol. 15, no. 2616, 2025.
- [3] T. K. V. Dai, “Remote human vital sign monitoring using MIMO radar at millimeter-wave frequencies,” Ph.D. dissertation, University of Tennessee, 2022.
- [4] Z. Xu *et al.*, “Simultaneous monitoring of multiple people’s vital sign leveraging a single phased-MIMO radar,” *IEEE J. Electromagnetics, RF and Microwaves in Medicine and Biology*, vol. 6, no. 3, pp. 311–324, 2022.
- [5] J. Metcalf, “Lecture 18: Introduction to moving-target indication,” 2024.



(a)



(b)



(c)

Figure 1: Laboratory set-up: radar (centre left) at chest height, ECG + IP electrodes (hidden under shirt).

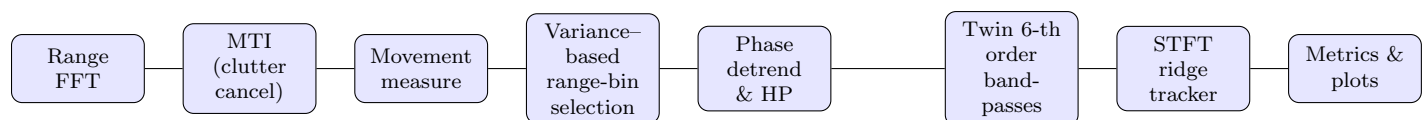


Figure 2: Processing chain A: band-pass + STFT back-end.

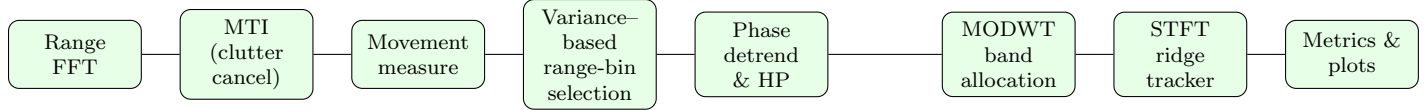
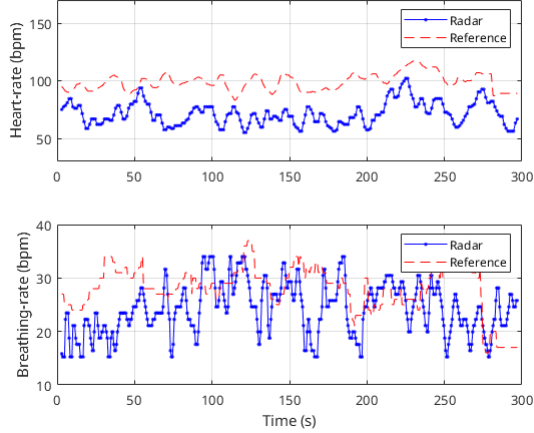
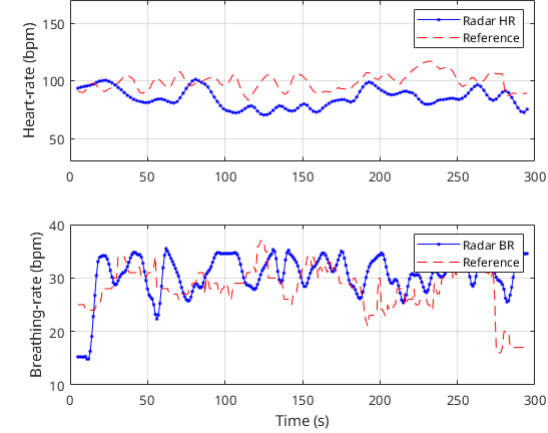


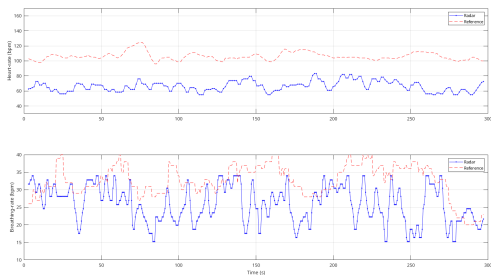
Figure 3: Processing chain B: MODWT + STFT back-end.



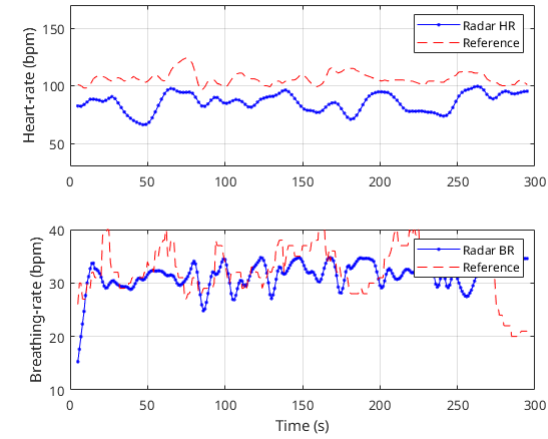
P01 – band-pass branch (A). The radar HR (blue) drifts 15–25 bpm below the reference (red) between throughout the collect; breathing-rate spikes coincide with the largest HR dips.



P01 – wavelet branch (B). Removing BR harmonics lifts the HR curve; the average gap to the reference shrinks from 19 bpm to 7 bpm and the BR curve loses the high-frequency jitter visible above.

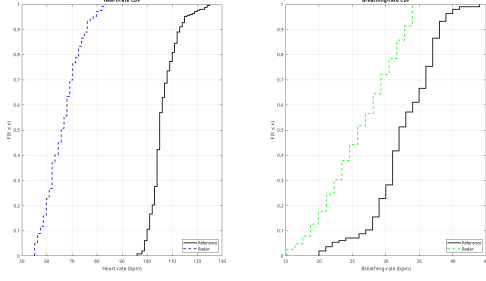


P02 – band-pass branch (A). Large dips at periodically in BR estimates compare to reference. HR estimates below the referenced HR. It ranges from 55 BPM to 79 BPM. Twice as low as the referenced estimates

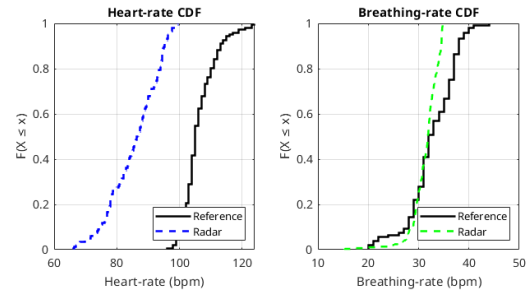


P02 – wavelet branch (B). Wavelet separation confines those motion bursts to a single scale; both HR and BR follow the reference envelopes within ± 8 bpm and ± 5 bpm, respectively.

Figure 4: Instantaneous HR/BR estimates (blue) against medical reference (red). Wavelet processing consistently closes the heart-rate bias and stabilises the breathing-rate line.

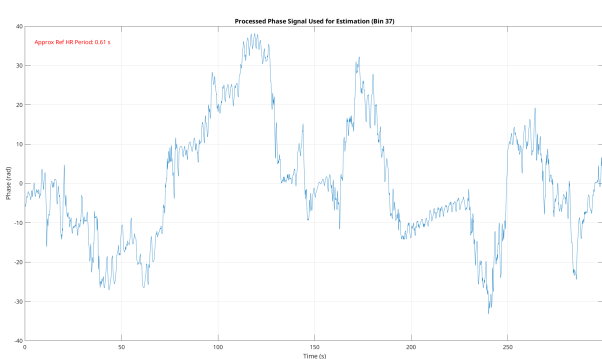


Absolute-error ranks – P02, band-pass branch.

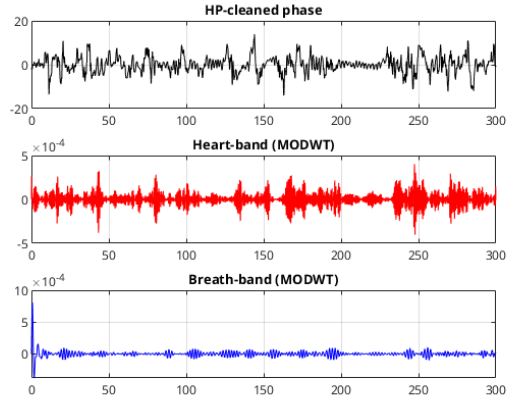


Absolute-error ranks – P02, wavelet branch.

Figure 5: Rank-ordered absolute errors for two children. Steeper curves indicate a larger fraction of small errors.

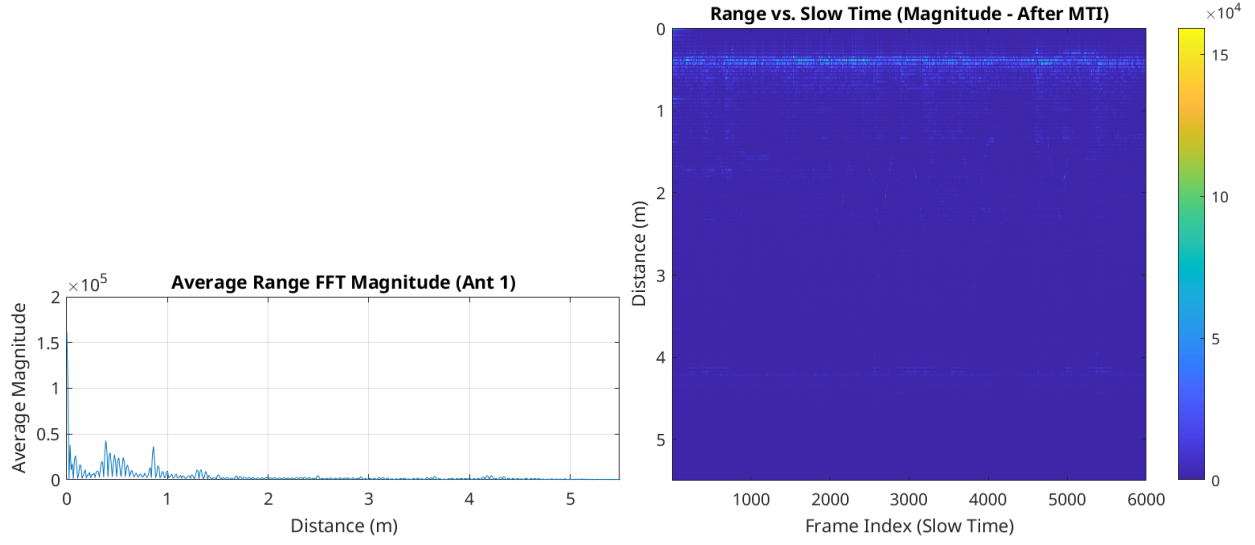


Drift-compensated phase for P01. Heart-beat ripples stand out only after removing low-frequency components.



MODWT decomposition of the same signal.

Figure 6: Backend-agnostic diagnostics used to tune filter settings and confirm proper scale selection.



(a) Fast-time range FFT magnitude of the *first* frame; (b) Stage-2 MTI waterfall $|M_1[r, k]|$ (dB) – static clutter is suppressed by ≈ 45 dB.

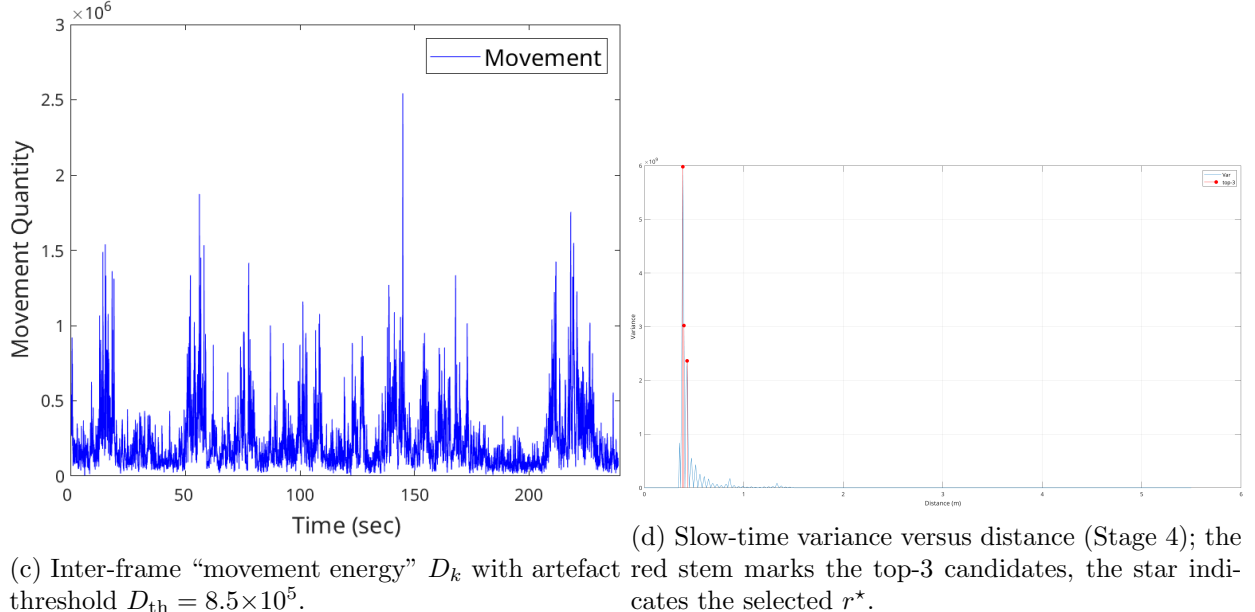


Figure 7: Radar front-end diagnostics for participant 1.